available at www.sciencedirect.com

ScienceDirect

journal homepage: www.elsevier.com/locate/jmbbm

ELSEVIER

Research paper

Constitutive modeling of porcine liver in indentation using 3D ultrasound imaging

P. Jordan[a,c], S. Socrate[b], T.E. Zickler[a], R.D. Howe[a,c,*]

[a] Harvard School of Engineering and Applied Sciences, Cambridge, MA, USA
[b] Massachusetts Institute of Technology, Department of Mechanical Engineering, Cambridge, MA, USA
[c] Harvard-MIT Division of Health Sciences and Technology, Cambridge, MA, USA

ARTICLE INFO

ABSTRACT

In this work we present an inverse finite-element modeling framework for constitutive modeling and parameter estimation of soft tissues using full-field volumetric deformation data obtained from 3D ultrasound. The finite-element model is coupled to full-field visual measurements by regularization springs attached at nodal locations. The free ends of the springs are displaced according to the locally estimated tissue motion, and the normalized potential energy stored in all springs serves as a measure of model-experiment agreement for material parameter optimization. We demonstrate good accuracy of estimated parameters and consistent convergence properties on synthetically generated data. We present constitutive model selection and parameter estimation for perfused porcine liver in indentation, and demonstrate that a quasilinear viscoelastic model with shear modulus relaxation offers good model-experiment agreement in terms of indenter displacement (0.19 mm RMS error) and tissue displacement field (0.97 mm RMS error).

1. Introduction

Computational models of organ and tissue mechanical response are beginning to play a significant role in modern computerized medicine and have become integral components of image-guided surgery and interventions (Carter et al., 2005; Clatz et al., 2005; DiMaio and Salcudean, 2005; Alterovitz et al., 2006; Cash et al., 2007; Archip et al., 2007). Such image-guided tasks require close interplay of computational biomechanical models with preoperative and intraoperative imaging. The development of appropriate models is challenging for two reasons. The first difficulty lies in the formulation of a suitable constitutive law capable of capturing the large-strain, nonlinear, viscoelastic response of tissues. The second challenge involves the development of experimental testing protocols appropriate for unique identification of the material parameters. In addition, the significant subject-to-subject variability contributes to a strong need for patient-specific (personalized) models, which may be generated and parameterized with clinically feasible testing protocols.

Material properties of soft tissues vary significantly between *in vivo* and *in vitro* settings (Fung, 1993; Miller and Chinzei, 1997; Miller et al., 2000; Gefen and Margulies, 2004; Miller, 2005; Kerdok et al., 2006). Current *in vivo* soft tissue

---

* Corresponding address: Harvard School of Engineering and Applied Sciences, 29 Oxford Street, Cambridge, MA 02138, USA. Tel.: +1 617 496 8359; fax: +1 617 495 9837.
E-mail address: howe@seas.harvard.edu (R.D. Howe).

testing is dominated by indentation due to the limited access requirements, simplicity of the instrumentation, and low risk of injury associated with the procedure (Balakrishnan and Socrate, 2008). The single force–displacement history obtained during conventional indentation experiments is governed by the mechanical response of the whole material domain, combining near-field (large strain) and far-field (low strain) contributions. Much of the information related to the interplay between shear and bulk compliance in the complex deformation field beneath the indenter is lost when capturing this single output. Therefore, supplemental experimental methods, such as secondary indentation sensors (Balakrishnan and Socrate, 2008), tissue surface tracking (Einstein et al., 2005; Evans et al., 2007), or independent tests of bulk compliance (i.e. confined tissue compression) are necessary for well-conditioned parameter identification. Image-based characterization methods are a promising solution, as they provide the means for noninvasive, *in vivo* estimation of material parameters and offer improved sensitivity and uniqueness of recovered parameters.

In this paper, we propose a general inverse finite-element modeling framework for constitutive modeling and parameter estimation of soft tissues using full-field volumetric deformation data obtained from 3D ultrasound. We validate the parameter estimation method on synthetically generated data and perform constitutive model selection for perfused porcine liver in indentation. While we limit our investigation to an experimental protocol which involves a single indenter displacement rate, the volumetric imaging captures local tissue strain rates in the range from zero to the maximum rate beneath the indenter. By exploring agreement with the image-based internal tissue displacement field, we determine an appropriate constitutive law and material parameters, which capture the time-dependent response of the tissue.

2. Methods

In this paper we describe a liver indentation experimental system and an inverse finite-element modeling framework, which takes advantage of concurrent image data obtained from 3D ultrasound imaging. While the liver is an inhomogeneous organ with complex anatomical structure, our model approximates it as a homogeneous and isotropic material. The characteristic length of the hepatic lobules, the functional units of the organ, is on the order of 1 mm. Therefore, the concept of homogenizing the tissue is justifiable for deformation fields applied over longer length scales (approximately 1 cm). In this work we also neglect the effects of the liver capsule and minimize the contributions from vasculature by examining the parenchyma with 3DUS and avoiding the placement of the indenter over large vessels. The proposed approach relies on the following components: experimental indentation apparatus, volumetric imaging system, a nonrigid registration algorithm for deformation field estimation, and a nonlinear parameter optimization algorithm. The design considerations and performance of each component are described in the following sections. In

addition, we present a validation study and an application of this framework to constitutive modeling of perfused porcine liver in indentation.

2.1. Experimental setup

2.1.1. Liver perfusion apparatus
Due to changes in the liver's mechanical properties *ex vivo* (Kerdok, 2006; Nava et al., 2007), it is important to measure the organ response in its physiological conditions. Measurement of boundary conditions and instrument access are often the limiting factors in *in vivo* testing. To address these challenges, we used an *ex vivo* perfusion system, described by Kerdok (2006) and depicted in Fig. 1. This system allowed us to perform organ tests with control of boundary conditions and near *in vivo* tissue state. The whole porcine liver was perfused with a heated perfusate (five liters of Dextrose 5% Lactated Ringers Solution (D5RL) and one liter of 6% Hetastarch (Henry Schein, Melville, NY)) under physiologic pressures, with a mean portal venous pressure of 7.98 mmHg, a mean hepatic arterial pressure of 94.77 mmHg, and at a mean temperature of 33 °C.

Following the experimental protocol described in Kerdok et al. (2006) and Kerdok (2006), the liver was indented at 2 mm/s to a depth of 9.2 mm with a 12 mm diameter, flat, cylindrical indenter actuated by Electroforce ELF 3200 (Bose Corporation EnduraTEC Systems Group, Minnetonka, MN, USA) material testing system. The system measures displacement using a linear variable differential transformer (Schaevitz MHR-250, Measurement Specialties, Hampton, VA, USA) with ± 6.3 mm travel (0.559 μm RMS alone, 3.9 μm RMS with controller), force using a 22 N submersible load cell (0.49 mN RMS alone, 13 mN RMS with controller) (Honeywell Sensotec Sensors Model 31, Columbus Ohio), and acceleration using a ± 50 g accelerometer (0.024 V RMS alone, 0.204V RMS with controller) (Kistler, Amherst, NY, USA).

2.1.2. Volumetric imaging
The volumetric deformation was imaged with the 3D ultrasound probe (SONOS 7500, Philips Medical Systems, Andover, MA, USA) placed below the tissue sample, as shown in Fig. 1. The 2–4 MHz probe acquires data at the rate of 26 frames per second, which is subsequently streamed over an Ethernet connection to a PC workstation for storage and processing. The transducer was operated at a 7 cm depth of focus to provide sufficient field of view, which contains the organ surface, parenchyma, and the probe stand-off pad. The resulting volumetric frames were rasterized at $128 \times 48 \times 204$ voxels, corresponding to an axial resolution of approximately 0.3 mm/voxel and a lateral resolution of 0.5 mm/voxel. Two-dimensional image slices of the volumetric sequence and the associated indenter force and displacement histories, acquired during a 2 mm/s load/unload cycle, are shown in Fig. 2.

2.2. Nonrigid image registration and full-field constitutive modeling

We use a nonrigid registration scheme (Fig. 3), described in further detail in Jordan et al. (2008), to estimate the deformation field captured by the concurrent 3DUS imaging.
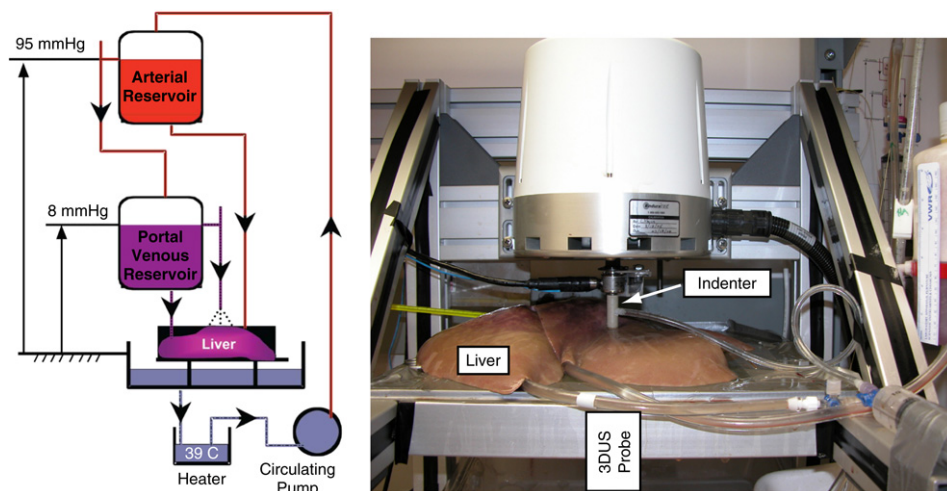
Fig. 1 – Left: liver perfusion system. Right: the experimental arrangement showing the indenter at the top surface of the organ and the 3DUS probe beneath the organ.
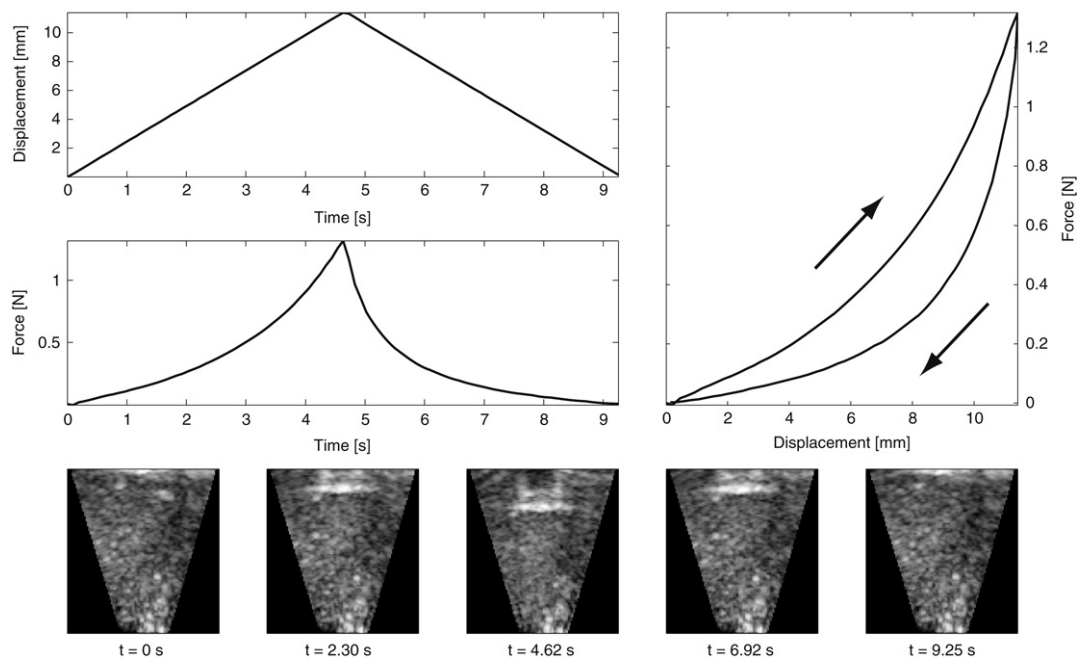

Fig. 2 – The indenter force and displacement histories and force–displacement indentation response, acquired during 2 mm s^{-1} load/unload cycle. The associated 2D slices through the 3DUS sequence are shown at the bottom.

The volumetric image data obtained during organ indentation contains relatively slow deformations (maximum tissue displacement is less than 0.3 voxels per frame) and the liver parenchyma produces rich textural content under 3DUS (see Fig. 2). Given these conditions, the algorithm achieves good accuracy and robustness. In Jordan et al. (2008) we demonstrate the accuracy against manually tracked tissue landmarks (mean magnitude error of less than 0.6 mm) in *ex vivo* liver indentation and present a quantitative error analysis using synthetic deformation sequences.

In the proposed nonrigid image registration scheme, sparse image-based local motion estimates u^{OF} and associated confidence c^{OF} are estimated with an adaptation of the Lucas and Kanade (1981) optical flow algorithm described

in Appendix. These local motion estimates are enforced as concentrated forces applied at the nodes of a deformable finite-element organ model, enforcing physically admissible deformations. The concentrated forces are generated by regularization springs, connected to the mesh nodes, as their free ends are displaced according to local motion estimates. The choice of each regularization spring stiffness reflects local textural quality and associated local motion confidence. This approach not only provides regularized estimate of organ deformation field (u^{FEM}) but also offers a measure of model/experiment agreement in the form of normalized potential energy (Φ) contained in regularization springs. The displacement field u^{FEM} is the equilibrium field computed by
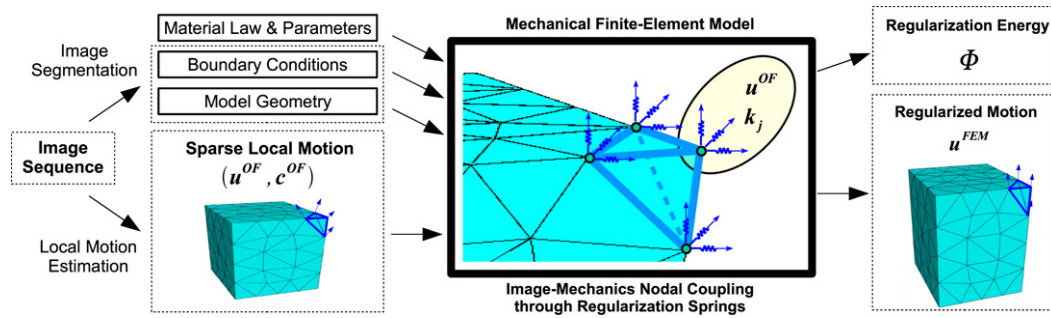
Fig. 3 – In the nonrigid image registration framework, sparse local motion estimates u^{OF} are coupled to a mechanical finite-element model as lumped body forces applied by displaced regularization springs. This results in a mechanically constrained deformation field u^{FEM} and regularization energy Φ.

the finite-element solver, minimizing the total potential energy of the system, which includes the strain energy stored in the continuum model and the potential energy in the regularization springs. Consequently, noisy $\mathbf{u}^{FEM}$ fields are penalized by the strain energy associated with the high local displacement gradients of the continuum model and excessively smoothed $\mathbf{u}^{FEM}$ fields are penalized by the increased potential energy of the regularization springs defined as

$$U_S = \sum_{i=1}^{N} \sum_{j} \left(\frac{1}{2} \mathbf{k}_j^i \left(\mathbf{d}_j^i \right)^2 \right), \tag{1}$$

where $j = \{x, y, z\}$, N is the number of attached regularization springs, $\mathbf{k}_j^i$ is the spring stiffness, and the spring distension $\mathbf{d}_j^i$ is defined as $\mathbf{d}_j^i = \mathbf{u}^{OF} - \mathbf{u}^{FEM}$. In order to relate the image-based confidence values to physically relevant springs stiffnesses, each stiffness is obtained not only as a function of local image texture, but also of the local nodal stiffness of the mechanical model. Therefore, the stiffness of each regularization spring is computed as

$$\mathbf{k}_j^i = \beta \mathbf{K}_j^i \mathbf{c}_{ij}^{OF}, \tag{2}$$

where i is the node index, β is the regularization coefficient, and $\mathbf{K}_j^i$ is the global stiffness of node i in direction j (obtained from the diagonal members of the global stiffness matrix).

The image registration framework is suitable for two types of fundamentally different applications. In the first category of applications, the framework may be used to obtain a mechanically admissible image registration, such as between preoperative and intraoperative images. In these applications, the biomechanical model and the image similarity term are coupled via the regularization springs to provide mechanically consistent internal organ deformations. Examples of such applications include the intraoperative brain shift, tumor localization, mammogram registration, etc. The second category consists of applications in constitutive organ response characterization. When external forces and boundary conditions are known or experimentally measured, the registration framework may be used to optimize the consistency between the chosen biomechanical model and the experimental images. When measuring the constitutive response of an organ, an objective function $\Phi(\mathbf{p}_n)$ derived from the springs potential energy U_S, may be defined as

$$\Phi(\mathbf{p}_n) = \sum_{i=1}^{N} \sum_{j} \left(\frac{\frac{1}{2} \mathbf{k}_j^i \left(\mathbf{d}_j^i \right)^2}{\frac{1}{2} \beta \mathbf{K}_j^i} \right) = \sum_{i=1}^{N} \mathbf{c}_i^{OF} \left(\mathbf{u}_i^{OF} - \mathbf{u}_i^{FEM} \right)^2 \tag{3}$$

and serves as an appropriate measure of model-experiment agreement. The energy is normalized by the nodal stiffness $\mathbf{K}_j^i$ to prevent artificial bias towards compliant models. Additionally, the spring energy is normalized by the regularization coefficient β. This parameter determines the image-mechanics coupling balance in the conventional image registration applications. When modeling the constitutive response of an organ, we seek to identify mechanical models which are consistent with the local unregularized motion estimates $\mathbf{u}^{OF}$. Therefore, the choice of parameter β does not affect the model-experiment fitting.[1] Using the objective function $\Phi(\mathbf{p}_n)$ defined in Eq. (3), imperfect models are associated with higher levels of regularization energy. The magnitude of the regularization energy, therefore, can be considered a measure of the accuracy of a constitutive formulation, and minimization algorithms can be used to determine optimal material parameters.

In our experimental configuration, the force and displacement histories at the tip of the indenter are acquired with higher accuracy and lower noise in comparison to the optical flow measurements. To incorporate these sensor measurements into the optimization framework, we define an objective function $\dot{\Phi}$, which is the sum of a volumetric error term $\dot{\Phi}_{vol}$ and an indenter error term $\dot{\Phi}_{ind}$ defined as

$$\dot{\Phi}_{vol}(\mathbf{p}_n) = \frac{1}{NT} \int_0^T \sum_{i=1}^{N} \mathbf{c}_i^{OF}(t) \left(\dot{\mathbf{u}}_i^{OF}(t) - \dot{\mathbf{u}}_i^{FEM}(t) \right)^2 dt \tag{4}$$

and

$$\dot{\Phi}_{ind}(\mathbf{p}_n) = \frac{1}{T} \int_0^T \left(\dot{\mathbf{u}}_z^{exp}(t) - \dot{\mathbf{u}}_z^{model}(t) \right)^2 dt. \tag{5}$$

The volumetric error term $\dot{\Phi}_{vol}$ is the mean squared difference between the optical flow and the model velocity fields over the time period T normalized by the number of regularization springs N. The indenter error term $\dot{\Phi}_{ind}$ is the mean squared difference between the vertical indenter velocity $\dot{\mathbf{u}}_z^{exp}(t)$ and the modeled indenter velocity $\dot{\mathbf{u}}_z^{model}(t)$. Such definition of the objective function scales the two error

---

[1] The role of the regularization parameter (and corresponding spring stiffness) is significant in scenarios where the framework is used for estimation of the internal organ deformation fields (i.e. brain shift problems, liver tumor localization, etc.). Details regarding these applications may be found in Jordan et al. (2008).
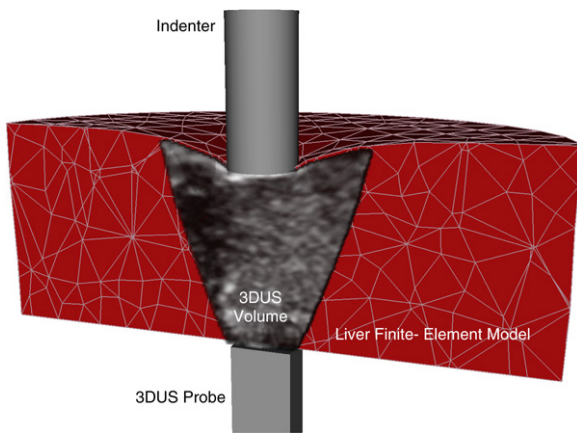
Fig. 4 – The deforming finite-element liver model with simplified cylindrical geometry, experimentally measured boundary conditions, and a coregistered 3DUS sequence.

components to comparable magnitudes and aids in obtaining model fits consistent with experimental tissue displacement field as well as the indenter force–displacement history.

Throughout this paper, we chose to use indenter and nodal velocity histories as the measure of model-experiment agreement. Objective functions based on velocity-based or displacement-based model-experiment agreement are both suitable choices for model optimization. The differential optical flow estimates are frame-to-frame displacement estimates (not absolute). Therefore, small estimation errors may contribute to more significant accumulation error (Lim and El Gamal, 2001) when integrated over long periods of time. For this reason, we determined the velocity fields as the more appropriate choice and were able to confirm their improved convergence properties.

2.2.1. Liver finite-element model

The perfused *ex vivo* liver is modeled with a finite-element model implemented in a commercial FE solver (ABAQUS 6.7, Simulia, Providence, RI, USA). The model has a simplified cylindrical geometry (10.0 cm diameter, 3.03 cm height) shown in Fig. 4, as most of the contributions to the indentation response are assumed to be local and not significantly dependent on the whole organ geometry. The mesh is generated automatically with increased density beneath the indenter and consists of 1424 nodes and 804 quadratic tetrahedral elements. The bottom surface of the organ is fully constrained, while the upper and side surfaces are assumed to be stress-free boundaries. The force at the tip of the indenter is prescribed to match the indentation force history obtained experimentally.

2.3. Method validation: Synthetic volumetric data

To evaluate the sensitivity of the testing method to material parameters, accuracy of the parameters recovered, and to assess the convergence characteristics of the optimization scheme, we conducted a parameter identification study on a synthetically generated 3DUS sequence. We computed a ground-truth deformation field from a forward finite-element

model of the indentation experiment with assumed constitutive law and material parameters. We used a high density mesh (4281 nodes, 2706 quadratic tetrahedral elements) in the forward model to minimize field discretization artifacts. The boundary conditions of the forward model were prescribed to match the boundary conditions of the real experimental procedure. The displacement and force histories at the tip of the indenter were recorded to mimic the measurements obtained during the *ex vivo* experimental procedure. The resulting deformation field was used to warp a reference 3DUS volume, generating a sequence of 100 volumes. The reference 3DUS volume is a single frame acquired by imaging perfused *ex vivo* liver. Consequently, the generated volumetric sequence preserves the true texture and intensity distribution of liver parenchyma under 3DUS. This synthetic study, however, excludes image artifacts and noise contributions from the imaging sensor.

2.3.1. Biphasic poroelastic constitutive law

To mimic the nonlinear viscoelastic response of the perfused porcine liver, we use a biphasic (mixture theory) constitutive model (Suh and Spilker, 1994; Zhu and Wang, 1998). Biphasic models account for viscous material effects through momentum exchange effects between the solid and fluid phases. The solid phase is formulated through the 2nd-order reduced polynomial strain-energy defined as

$$U = C_1 \left(I_1 - 3\right) + C_2 \left(I_1 - 3\right)^2 + \frac{1}{D_1} \left(J_{el} - 1\right)^2 \qquad (6)$$

where C_1, C_2, and D_1 are the material parameters, I_1 is the 1st stretch invariant, and J_{el} is the elastic volumetric stretch. The flux of the fluid phase is governed by Darcy's law expressed as

$$\mathbf{q} = \kappa \nabla \mathbf{P}, \qquad (7)$$

where $\mathbf{q}$ is the flux, κ is the permeability coefficient, and $\nabla \mathbf{P}$ is the fluid pressure gradient.

Using the synthetic 3DUS sequence and force–displacement indentation histories, we perform material parameter estimation in a way that is identical to the approach used with true experimental liver measurements. The geometry and boundary conditions of the FE model used in this inverse process reflect the assumed experimental conditions. The indentation force $F(t)$ is applied at the tip of the indenter, and the bottom surface of the organ is fully constrained. We initialize material parameters with feasible parameter estimates and use a nonlinear optimization algorithm, a bounded downhill simplex method (Lagarias et al., 1998), to iteratively evolve the material parameters (C_1, C_2, D_1, κ) and minimize the objective function $\dot{\Phi}(\mathbf{p}_n)$.

2.3.2. Quasilinear viscoelastic constitutive law

In the second synthetic parameter recovery study we perform parameter identification using an alternative constitutive material law, a 2nd-order reduced form polynomial hyperelastic law with a Prony series relaxation of the shear modulus (Holzapfel, 2000; Hibbit, Karlsson, Sorensen, 2007). The hyperelastic strain energy of this constitutive law defined in Eq. (6) and the relaxation of the shear modulus $G(t)$ is captured by a 1st-order Prony series

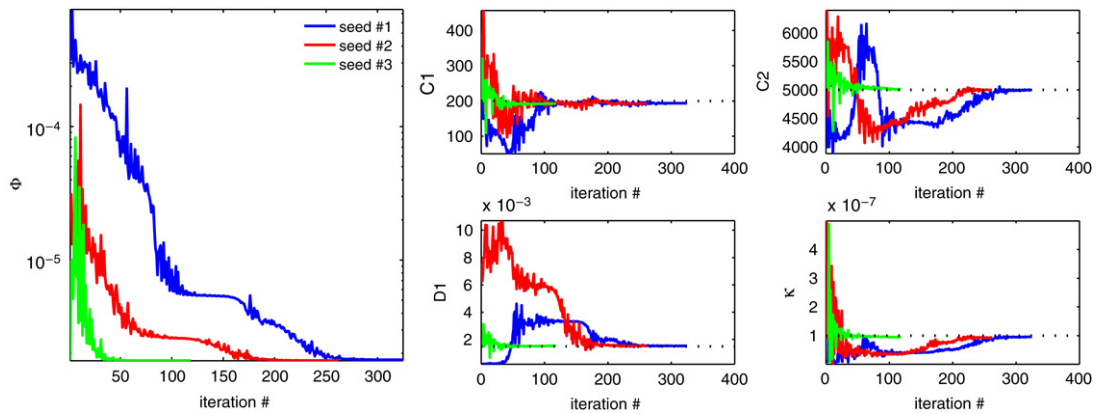$$G(t) = G_0 \left(g_\infty + g_1 e^{-t/\tau_{g1}}\right), \qquad (8)$$

Fig. 5 – Biphasic poroelastic CL: regularization energy evolution (left) and material parameter evolution (right) during material parameter identification seeded from 3 different locations in the parameter space.

where G_0 is the instantaneous shear strain modulus (computed from Eq. (6)), $G_0 g_\infty$ is the equilibrium shear strain modulus, $g_1 = 1 - g_\infty$ is the relative amplitude of the relaxation, and τ_{g1} is the relaxation time constant. The biphasic poroelastic constitutive law governing the response of the synthetic deformation is known to exhibits bulk relaxation. We evaluate the volumetric agreement with a shear relaxation constitutive law to demonstrate the ability to distinguish between materials with inherently different modes of relaxation. We also evaluate the method's ability to consistently converge to the best possible fit under the given assumptions.

2.4. Perfused porcine liver constitutive modeling

We perform constitutive modeling of perfused porcine liver in indentation (2 mm s^{-1} load/unload cycle) using the proposed inverse modeling framework. We constrain our attention to the 2nd-order reduced polynomial hyperelastic form

$$U = C_1 (I_1 - 3) + C_2 (I_1 - 3)^2 + \frac{1}{D_1} (J_{el} - 1)^2 + \frac{1}{D_2} (J_{el} - 1)^4 \quad (9)$$

and shear and bulk relaxation components

$$G(t) = G_0 \left(g_\infty + g_1 e^{-t/\tau_{g1}} \right) \quad (10)$$

$$K(t) = K_0 \left(k_\infty + k_1 e^{-t/\tau_{k1}} \right). \quad (11)$$

Under this general form, we explore 5 constitutive laws. In the shear relaxation variant (SR), the relaxation of the tissue is assumed to be captured by the relaxation of the instantaneous shear modulus. The bulk compliance is assumed to be linear ($D_2 = 0$) and no bulk relaxation is permitted ($k_1 = 0$). In the subsets SR$_{low}$ and SR$_{high}$ we enforce low ($D_1 = 1.0 \times 10^{-4}$) and high ($D_1 = 3.0 \times 10^{-3}$) bulk compliance, respectively, to investigate the effects of bulk compliance on the full-field deformation fields.

To investigate the role of bulk relaxation we consider two additional constitutive laws. First, we consider a bulk relaxation (BR) model with 2nd- order bulk compliance and no shear relaxation ($g_1 = 0$). Second, we considered the full constitutive law (SBR) with relaxation of both bulk and shear moduli.

3. Results

3.1. Method validation: Synthetically generated volumetric data

3.1.1. Biphasic poroelastic constitutive law
Using the synthetically generated deformation sequence governed by biphasic poroelastic constitutive law, the parameter estimation framework consistently converges to the ground-truth parameter values. The evolution of the objective function during the optimization processes seeded from 3 distinct points in the parameter space is shown in Fig. 5, left. The convergence of the material parameters for all 3 seeds is shown in Fig. 5, right. These results are summarized in Table 1 and demonstrate that in the absence of imaging noise (a consequence of synthetic data) the method converges consistently and recovers both bulk and shear response parameters with good sensitivity.

3.1.2. Quasilinear viscoelastic constitutive law
The parameter estimation of the quasilinear viscoelastic constitutive law using the deformation sequence with assumed biphasic poroelastic response is summarized Fig. 6 and Table 2. These results suggest that the method converges consistently for all 3 seed points and is able to obtain excellent indenter response agreement with the ground-truth data (see Fig. 7). However, when comparing the magnitudes of the volumetric error, this form of constitutive law offers lesser volumetric agreement with the data. This point is further illustrated by comparing the nodal velocities of the poroelastic (PE), viscoelastic (VE), and optical flow data in Fig. 8. Since the PE model corresponds to the ground-truth deformation, Fig. 8 demonstrates the volumetric disparity of the VE model. In addition, the good agreement of the optical flow estimates with the PE model serves as a validation of the motion estimation scheme (in the absence of imaging system noise). In addition, it serves as a basis for measuring the noise floor of the motion estimation system. Minor oscillations in the optical flow estimates may be observed at some nodes due to voxel-to-element correspondence effects near the model boundary.

Table 1 – Biphasic poroelastic CL: recovered material parameters and associated regularization energy obtained from 3 independent parameter seed points (initial parameter values shown in parentheses)

Parameter	Seed 1	Seed 2	Seed 3
C_1	193.6 (150)	192.4 (300)	192.7 (200)
C_2	4998 (4000)	4999 (6000)	5014 (5000)
D_1	1.53×10^{-3} (2.0×10^{-4})	1.53×10^{-3} (5.0×10^{-3})	1.53×10^{-3} (1.5×10^{-3})
κ	0.96×10^{-7} (1.0×10^{-8})	0.93×10^{-7} (5.0×10^{-7})	0.95×10^{-7} (1.0×10^{-7})
$\dot{\Phi}$	2.63×10^{-6} (6.39×10^{-6})	2.63×10^{-6} (9.10×10^{-6})	2.63×10^{-6} (2.65×10^{-6})
$\dot{\Phi}_{\mathrm{ind}}$	1.08×10^{-8} (2.54×10^{-6})	1.23×10^{-8} (5.12×10^{-6})	1.22×10^{-8} (1.70×10^{-8})
$\dot{\Phi}_{\mathrm{vol}}$	2.62×10^{-6} (3.85×10^{-6})	2.62×10^{-6} (3.98×10^{-6})	2.62×10^{-6} (2.63×10^{-6})

Ground-truth values: $C_1 = 200$, $C_2 = 5000$, $D_1 = 1.5 \times 10^{-4}$, $\kappa = 1.0 \times 10^{-7}$.

Table 2 – Viscoelastic CL: recovered material parameters and associated regularization energy obtained from 3 independent parameter seed points (initial parameter values shown in parentheses)

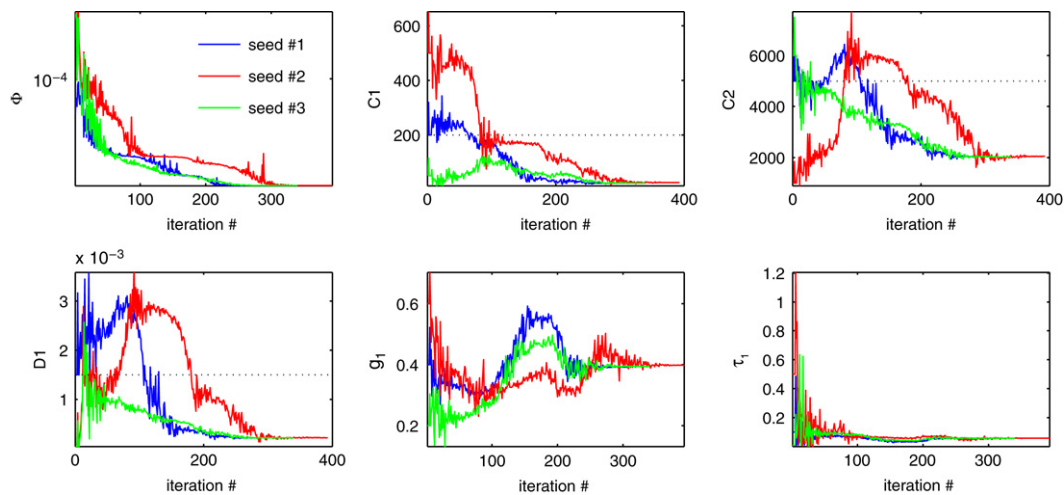| Parameter	Seed 1	Seed 2	Seed 3
C_1	23.1 (200)	24.9 (500)	23.1 (50)
C_2	2039 (5000)	2048 (1000)	2030 (6000)
D_1	2.25×10^{-4} (1.5×10^{-3})	2.27×10^{-4} (1.0×10^{-4}))	2.24×10^{-4} (5.0×10^{-5})
g_1	0.392 (0.400)	0.398 (0.600)	0.394 (0.200)
τ_1	0.059 (0.100)	0.058 (0.500)	0.059 (0.010)
$\dot{\Phi}$	1.57×10^{-5} (1.90×10^{-5})	1.51×10^{-5} (1.07×10^{-4})	1.56×10^{-5} (6.01×10^{-5})
$\dot{\Phi}_{\mathrm{ind}}$	9.32×10^{-6} (1.13×10^{-5})	8.82×10^{-6} (9.87×10^{-5})	9.18×10^{-6} (5.54×10^{-5})
$\dot{\Phi}_{\mathrm{vol}}$	6.39×10^{-6} (7.79×10^{-6})	6.32×10^{-6} (7.79×10^{-6})	6.38×10^{-6} (4.69×10^{-6})

Fig. 6 – Quasilinear viscoelastic CL: regularization energy evolution (top left) and material parameter evolution during material parameter identification seeded from 3 different locations in the parameter space.

3.2. Perfused porcine liver constitutive modeling

The results of the constitutive modeling of perfused porcine liver are summarized in Table 3 and Fig. 9. Several observations should be noted regarding the methods ability to characterize the material response and its contributions in the constitutive law selection process.

The results of the quasilinear viscoelastic constitutive law with shear modulus relaxation (SR) demonstrate that the proposed parameter identification method is capable of recovering the linear bulk compliance parameter D_1, which is not observable in conventional indentation tests. While the indentation response (Fig. 9 top middle) is nearly identical for all three SR models, the volumetric nodal velocities differ significantly. This disparity is captured by comparing the SR model's volumetric error term ($\dot{\Phi}_{\mathrm{vol}} = 2.15 \times 10^{-5}$) to the $\mathrm{SR}_{\mathrm{low}}$ ($\dot{\Phi}_{\mathrm{vol}} = 3.52 \times 10^{-5}$) and $\mathrm{SR}_{\mathrm{high}}$ ($\dot{\Phi}_{\mathrm{vol}} = 2.25 \times 10^{-5}$) models with assumed low and high bulk compliance D_1, respectively. These findings indicate that estimating the bulk compliance parameter D_1 from the full-field deformation data maximizes the volumetric model/experiment agreement.

The parameter identification results using the BR and SBR models suggest that bulk modulus relaxation does not significantly improve the model fit ($\dot{\Phi}_{\mathrm{vol}} = 3.8 \times 10^{-5}$ for BR, $\dot{\Phi}_{\mathrm{vol}} = 2.20 \times 10^{-5}$ for SBR). For this mode and rate of deformation the simple SR constitutive form is able to account for the material response both at the indenter as well as volumetrically (within the precision of the imaging and deformation tracking systems).
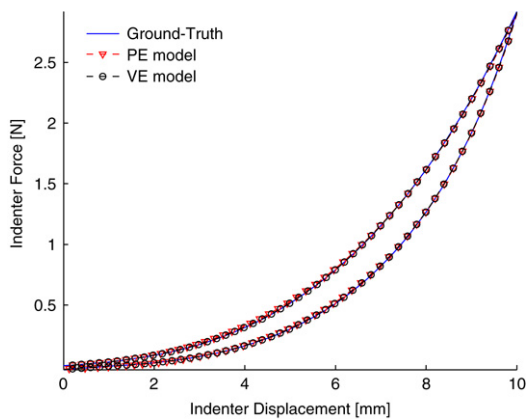
Fig. 7 – The force–displacement indentation response of the poroelastic model (PE) and viscoelastic model (VE) showing excellent agreement with ground-truth data.

The agreement between the model and the experiment was also quantified in terms of the root mean squared (RMS) error of the indenter and of the nodal displacement histories. While nodal velocity mean squared error (MSE) was found to be the more appropriate objective function choice for model optimization, the nodal displacement RMS errors provide an intuitive measure of the model-experiment agreement. Under this metric, the SR model offers good indenter displacement agreement (0.19 mm RMS error) and volumetric deformation agreement (0.97 mm axial RMS error).

4.   Conclusions

In this paper, we presented a method for constitutive model selection and parameter identification using real-time 3DUS volumetric imaging. This approach enriches the traditional force–displacement indentation response

with the measurement of volumetric deformation and provides good sensitivity to parameters governing the bulk response of the material. These parameters are otherwise not observable in conventional indentation. The ability to decouple the bulk and shear components of the deformation is important and we demonstrated that we can reconstruct the parameters with precision and repeatability in a validation study. Furthermore, the measurement of full volumetric deformation histories offers the ability to observe material response over a range of strain rates. While the indenter is driven at a chosen displacement rate, the local material strain rates throughout the tissue sample vary from zero in the far-field to the maximum levels beneath the indenter. The proposed method is independent of imaging modality and constitutive law, suggesting potential applications for other tissues and scales (i.e. nanoindentation, confocal microscopy, etc.).

The proposed approach is a useful tool for constitutive model selection, as suggested in our porcine liver indentation modeling. The best experimental fits were attained with a quasilinear viscoelastic model with 2nd-order reduced polynomial instantaneous response and a Prony series relaxation of the bulk and shear moduli. Using the full-field measurements, we demonstrated that a simpler constitutive form with shear relaxation provides comparable model-experiment agreement. This observation suggests that shear relaxation is the dominant mode of relaxation for liver in indentation and that the SR model is appropriate (considering the reduced number of parameters).

One of the advantages of the proposed method is the ease of application in *in vivo* settings. The knowledge/observation of boundary condition is one of the chief motivating factors for *ex vivo* testing. Imaging the organ during indentation testing, however, offers the ability to observe the *in vivo* boundary conditions and account for them during the inverse modeling process. Direct *in vivo* indentation tests of the liver can be performed in the operating room due to the relatively
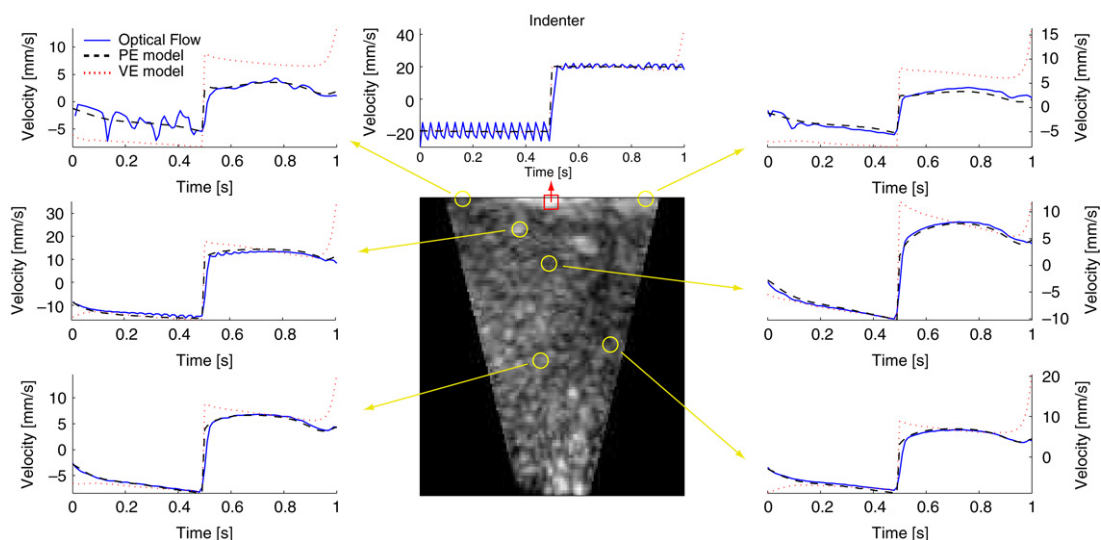

Fig. 8 – Ground-truth deformation sequence: mesh node velocity histories of the poroelastic (PE) and viscoelastic (VE) models compared to optical flow estimates. Only the vertical component of velocity is shown. The selected nodes are within 10 mm of the slice shown.
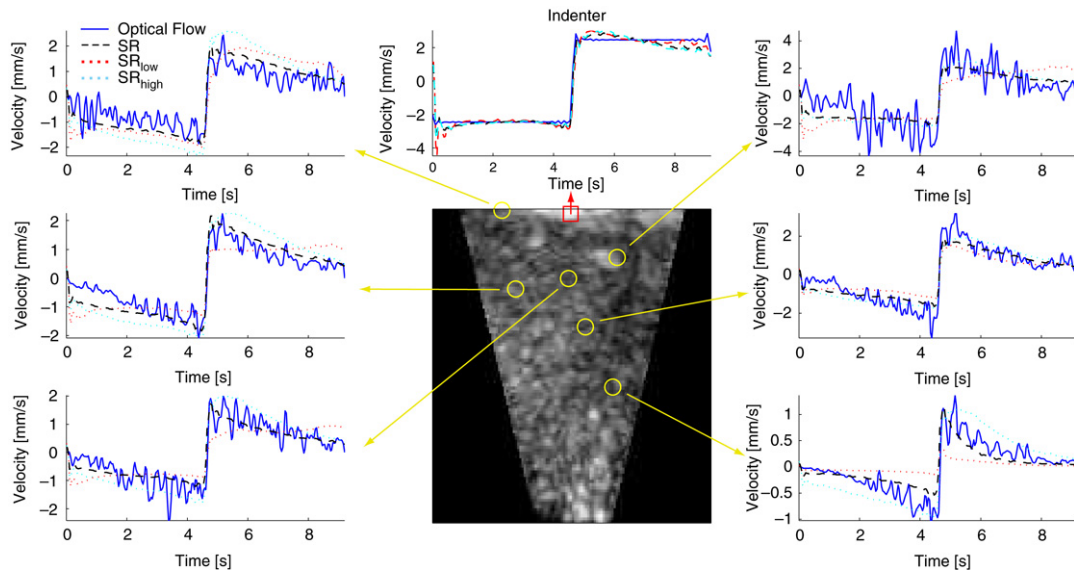
Fig. 9 – Perfused liver sequence: indentation histories (top, middle) are virtually identical between SR, SR_{low}, and SR_{high}. The SR model provides significantly improved volumetric agreement illustrated with vertical node velocity histories.

Table 3 – Perfused porcine liver: estimated material parameters for the 5 constitutive laws considered					
Parameter	SR_{low}	SR_{high}	SR	BR	SBR
C_1	4.3	185.4	79.2	83.9	71.6
C_2	47.0	612.6	257	40.9	218.3
D_1	1.0×10^{-4}	3.0×10^{-3}	4.38×10^{-4}	4.71×10^{-4}	3.65×10^{-4}
D_2	–	–	–	2.22×10^{-5}	6.7×10^{-3}
g_1	0.967	0.779	0.832	–	0.794
τ_{g1}	0.585	0.168	0.150	–	0.203
k_1	–	–	–	0.890	0.032
τ_{k1}	–	–	–	0.134	0.176
$\dot{\Phi}$	3.52×10^{-5}	2.25×10^{-5}	2.15×10^{-5}	3.08×10^{-5}	2.20×10^{-5}
$\dot{\Phi}_{ind}$	1.52×10^{-7}	1.69×10^{-7}	1.31×10^{-7}	1.58×10^{-7}	1.35×10^{-7}
$\dot{\Phi}_{vol}$	3.51×10^{-5}	2.24×10^{-5}	2.14×10^{-5}	3.06×10^{-5}	2.19×10^{-5}

easy access to the organ within the abdominal cavity. The method may also find suitable applications in noninvasive (percutaneous) organ characterization. Such applications will require proper image segmentation and mechanical models, which incorporate the tissue inhomogeneities, layers, and organ boundaries.

In our future work, we intend to incorporate constitutive laws with higher complexity (Kerdok et al., 2006; Mazza et al., 2007), which are capable of capturing the liver response across the DC-2 Hz frequency range characteristic of surgical manipulation.

Acknowledgements

Appendix. Local optical flow estimation

In this section we describe a modified Lucas-Kanade algorithm used for estimation of the local optical flow $\mathbf{u}^{OF}$. The traditional differential optical flow technique proposed by Lucas and Kanade (1981) relies on two fundamental assumptions: frame-to-frame intensity constancy and local intensity gradient constancy. Under these assumptions the motion of each voxel is constrained by the optical flow equation

$$\frac{\partial I}{\partial x}u_x + \frac{\partial I}{\partial y}u_y + \frac{\partial I}{\partial z}u_z + \frac{\partial I}{\partial t} = 0, \tag{A.1}$$

where $I(x, y, z, t)$ is the voxel intensity and $\{u_x, u_y, u_z\}$ are vector components of the voxel velocity. Since the optical flow constraint for a single voxel is ill-posed, the solution of the Lucas-Kanade algorithm relies on additional motion

assumptions within the local neighborhood. In our case we sample the neighborhood of each mesh node (all neighboring tetrahedra) and assemble a system of equations weighted by the corresponding elemental shape functions (see Zienkiewicz (1977) for the linear tetrahedral shape function definition).

$$N_i \frac{\partial I_i}{\partial x} u_x^{OF} + N_i \frac{\partial I_i}{\partial y} u_y^{OF} + N_i \frac{\partial I_i}{\partial z} u_z^{OF} = -N_i \frac{\partial I_i}{\partial t}. \tag{A.2}$$

Using the linear tetrahedral shape function as the nodal neighborhood weighting functions, the local system of optical flow equations can be rewritten as

$$\mathbf{A} u^{OF} = \mathbf{b}, \qquad \mathbf{A_{ij}} = N_i \frac{\partial I_i}{\partial j}, \quad \mathbf{b_i} = -N_i \frac{\partial I_i}{\partial t}, \tag{A.3}$$

where i is the voxel index and $j = \{x, y, z\}$. The nodal displacement can be recovered as the least-squares solution to this linear system. Local motion $\mathbf{u}^{OF}$ is computed at each mesh node, providing a globally unconstrained set of local motion estimates. Each nodal motion estimate has an associated confidence $\mathbf{c}^{OF}$. Traditionally, this confidence is computed from the three eigenvectors (direction of confidence) and eigenvalues (level of confidence) of the square $\mathbf{A}^T\mathbf{A}$ matrix. However, to account for the variability of local neighborhood size throughout the mesh, we follow an alternative approach in which we compute the texture-dependent confidence by summing the absolute values of image gradients in the nodal neighborhood, such that

$$c_j^{OF} = \sum_{i=1}^{n} N_i \left| \frac{\partial I_i}{\partial j} \right|, \tag{A.4}$$

where $i = \{1, \ldots, n\}$ are all voxels contained in elements surrounding the node of interest and $j = \{x, y, z\}$. The value of c_j^{OF} is subsequently normalized by the largest value contained in the image volume, such that $c_j^{OF} \in [0, 1]$.

REFERENCES

Alterovitz, R., Goldberg, K., Pouliot, J., Hsu, I.-C.J., Kim, Y., Noworolski, S.M., Kurhanewicz, J., 2006. Registration of mr prostate images with biomechanical modeling and nonlinear parameter estimation. Medical Physics 33 (2), 446–454.

Archip, N., Clatz, O., Whalen, S., Kacher, D., Fedorov, A., Kot, A., Chrisochoides, N., Jolesz, F., Golby, A., Black, P.M., Warfield, S.K., 2007. Non-rigid alignment of pre-operative MRI, fMRI, and DT-MRI with intra-operative MRI for enhanced visualization and navigation in image-guided neurosurgery. Neuroimage 35 (2), 609–624.

Balakrishnan, A., Socrate, S., 2008. Material property differentiation in indentation testing using secondary sensors. Experimental Mechanics 48 (4), 549–558.

Carter, T.J., Sermesant, M., Cash, D.M., Barratt, D.C., Tanner, C., Hawkes, D.J., 2005. Application of soft tissue modelling to image-guided surgery. Medical Engineering & Physics 27 (10), 893–909.

Cash, D.M., et al., 2007. Concepts and preliminary data toward the realization of image-guided liver surgery. Journal of Gastrointestinal Surgery 11 (7), 844–859.

Clatz, O., Delingette, H., Talos, I.-F., Golby, A., Kikinis, R., Jolesz, F., Ayache, N., Warfield, S., 2005. Robust nonrigid registration to capture brain shift from intraoperative MRI. IEEE Transactions on Medical Imaging 24 (11), 1417–1427.

DiMaio, S., Salcudean, S., 2005. Needle steering and motion planning in soft tissues. IEEE Transactions on Biomedical Engineering 52 (6), 965–974.

Einstein, D.R., Freed, A.D., Stander, N., Fata, B., Vesely, I., 2005. Inverse parameter fitting of biological tissues: A response surface approach. Annals of Biomedical Engineering 33 (12), 1819–1830.

Evans, S.L., Holt, C.A., Ozturk, H., Saidi, K., Shrive, N.G., 2007. Measuring soft tissue properties using digital image correlation and finite element modelling. In: Experimental Analysis of Nano and Engineering Materials and Structures. Springer Netherlands, pp. 313–314.

Fung, Y., 1993. Biomechanics: Mechanical Properties of Living Tissues, 2nd edition. Springer-Verlag, New York.

Gefen, A., Margulies, S.S., 2004. Are in vivo and in situ brain tissues mechanically similar? Journal of Biomechanics 37 (9), 1339–1352.

Hibbit, Karlsson, Sorensen, 2007. ABAQUS/Standard 6.7 User's Manual. Hibbit, Karlsson, & Sorensen, Pawtucket, RI.

Holzapfel, G.A., 2000. Nonlinear Solid Mechanics: A Continuum Approach for Engineering, 1st edition. Wiley.

Jordan, P., Zickler, T., Socrate, S., Howe, R., 2008. Modular nonrigid image registration framework using nonlinear mechanical regularization (in review). Medical Image Analysis.

Kerdok, A.E., 2006. Characterizing the nonlinear mechanical response of liver to surgical manipulation. Ph.D. Thesis, Harvard University.

Kerdok, A.E., Ottensmeyer, M.P., Howe, R.D., 2006. Effects of perfusion on the viscoelastic characteristics of liver. Journal of Biomechanics 39 (12), 2221–2231.

Lagarias, J.C., Reeds, J.A., Wright, M.H., Wright, P.E., 1998. Convergence properties of the Nelder-Mead simplex method in low dimensions. SIAM Journal of Optimization 9 (1), 112–147.

Lim, S., El Gamal, A., 2001. Optical flow estimation using high frame rate sequences. In: Proceedings of the International Conference on Image Processing, vol. 2. pp. 925–928.

Lucas, B.D., Kanade, T., 1981. An iterative image registration technique with an application to stereo vision. In: Proceedings of the 7th International Joint Conference on Artificial Intelligence (IJCAI '81). pp. 674–679.

Mazza, E., Nava, A., Hahnloser, D., Jochum, W., Bajka, M., 2007. The mechanical response of human liver and its relation to histology: An in vivo study. Medical Image Analysis 11 (6), 663–672.

Miller, K., 2005. Method of testing very soft biological tissues in compression. Journal of Biomechanics 38 (1), 153–158.

Miller, K., Chinzei, K., 1997. Constitutive modelling of brain tissue: Experiment and theory. Journal of Biomechanics 30 (11–12), 1115–1121.

Miller, K., Chinzei, K., Orssengo, G., Bednarz, P., 2000. Mechanical properties of brain tissue in-vivo: Experiment and computer simulation. Journal of Biomechanics 33 (11), 1369–1376.

Nava, A., Mazza, E., Furrer, M., Villiger, P., Reinhart, W.H., 2007. In vivo mechanical characterization of human liver. Medical Image Analysis.

Suh, J.-K., Spilker, R.L., 1994. Indentation analysis of biphasic articular cartilage: Nonlinear phenomena under finite deformation. Journal of Biomechanical Engineering 116, 1–9.

Zhu, C., Wang, C.-B., 1998. Biphasic Theory for Hydrated Soft Tissues. New York Orthopaedic Hospital Research Laboratory.

Zienkiewicz, O.C., 1977. The Finite Element Method, 3rd edition. McGraw-Hill.